Department of Precision and Microsystems Engineering

Air-based Contactless Wafer Precision Positioning System, Contactless Sensing Using Charge Coupled Devices

Rico Hooijschuur

Report no	: 2019.046
Coach	: Dr. N. Saikumar & Dr. S.H. HosseinNia
Professor	: Dr. Ir. R.A.J. van Ostayen
Specialisation	: Mechatronic System Design
Type of report	: Master Thesis
Date	: 18 December 2019

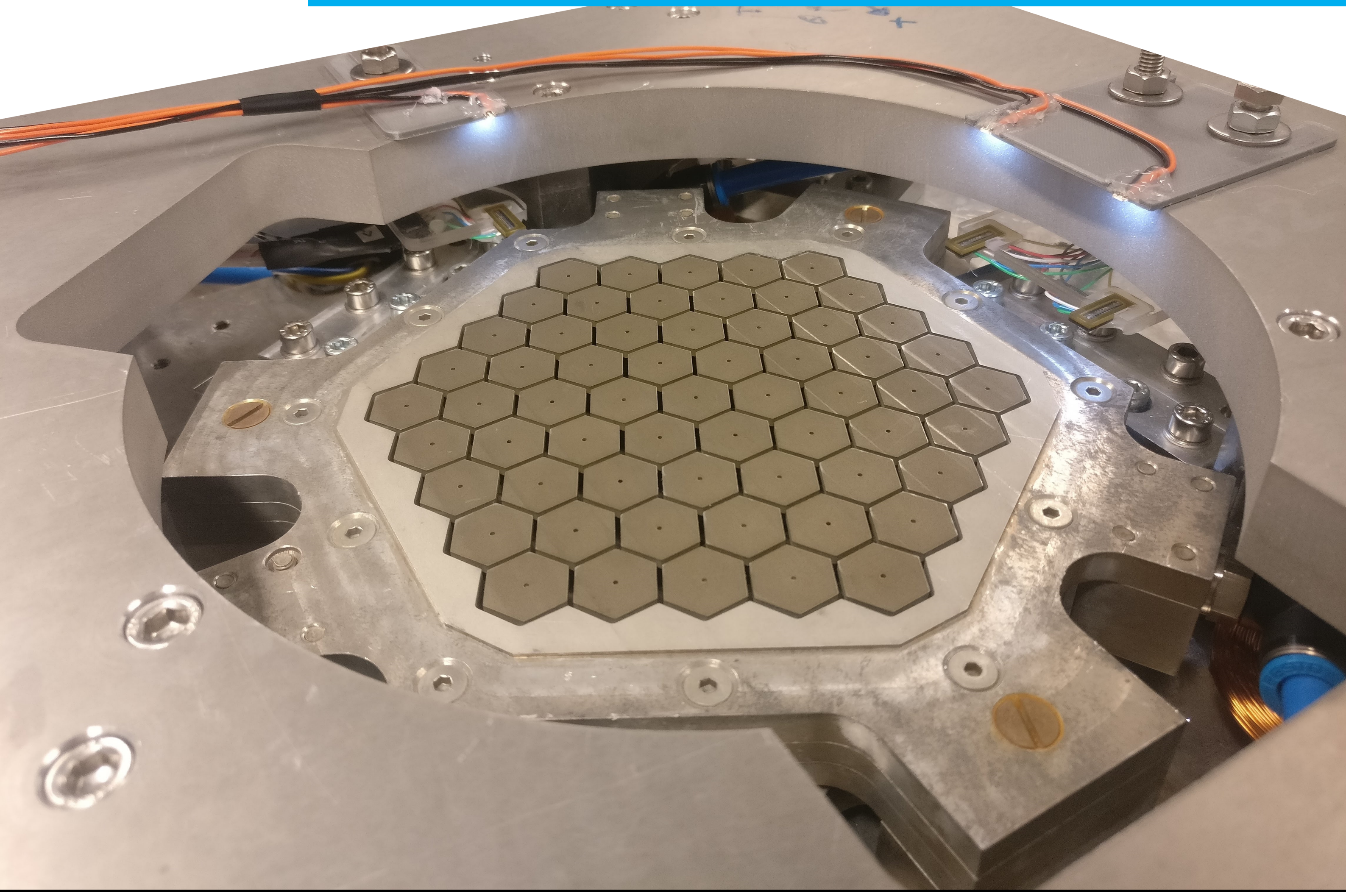

Delft University of Technology

Challenge the future

Air-based Contactless Wafer Precision Positioning System

Contactless Sensing Using Charge Coupled Devices

by

Rico Hooijschuur

to obtain the degree of Master of Science
at the Delft University of Technology,
to be defended publicly on Wednesday December 18, 2019 at 11:00 AM.

Student number:	4240294	
Project duration:	September, 2018 – December, 2019	
Thesis committee:	Dr. Ir. R.A.J. van Ostayen,	TU Delft, supervisor
	Dr. S.H. HosseinNia,	TU Delft
	Dr. F. Alijani,	TU Delft
	Prof. Dr. Ir. J.W. van Wingerden,	TU Delft

This thesis is confidential and cannot be made public until December 18, 2021.

TU Delft

Preface

In this section, I would like to express my gratitude to everyone who has contributed to my graduation project and who supported me along the way. When I started the project I was thrown in the deep with this high tech machine, the flowerbed. I really enjoyed figuring out how this machine works. Where its limitations lie and how these limitations could be overcome. Sometimes it was frustrating, not knowing why some effects occurred, but this made it even more rewarding when I did find what the problems were.

The first person I would like to thank is Niranjan Saikumar. Thank you, for the support as my daily supervisor. I learned a lot from your viewpoint and how you could clearly explain the theory. I would like to thank Hassan HosseinNia and Ron van Ostayen for introducing me to this fitting project. My gratitude also goes out to Jo Spronck for practical and technical advice and support.

I would like to thank the PME staff and the students, which were present during the feedback sessions. The critical view helped me to improve my work.

I would like my friends for the fun times, the support and coffee breaks. These helped me to clear the mind for new theories.

To my parents, who supported me throughout my journey in Delft and as last but not least, Alexandra for the patience and support during the long days.

Rico Hooijschuur
Delft, December 2019

Abstract

This thesis presents the development of a contactless sensing system and the dynamic evaluation of an air-bearing based precision wafer positioning system. The contactless positioning stage is a response to the trend seen in the high-tech industry, with the substrates becoming thinner and larger to reduce the cost and increase the yield. With contactless handling, it is possible to avoid damage and contamination. The system works by floating the substrate on a thin film of air. A viscous traction force is applied on the substrate by steering the airflow.

A cascaded control structure has been implemented in the contactless positioning system, where the Inner Loop Controller (ILC) controls the actuator which steers the airflow and the Outer Loop Controller (OLC) controls the position of the substrate by controlling the reference of the ILC. This is shown in Figure 1.

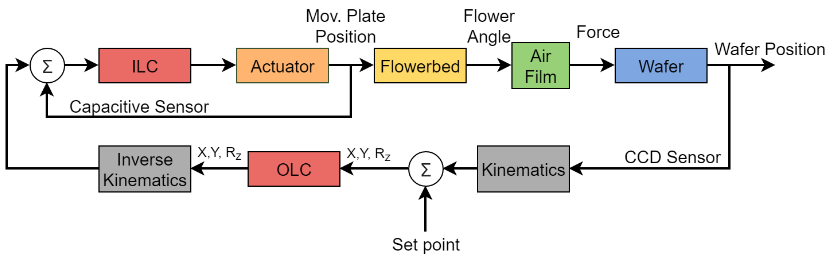

Figure 1: The control strategy for the flowerbed.

The dynamics of the ILC are evaluated and optimized for the performance of the positioning of the substrate. The bandwidth of the system has been improved from 233 to 300 Hz. The vibration disturbances are handled by the higher bandwidth ILC, as the air does not transmit the floor vibration disturbance. Furthermore, the origin of the phase lag which was limiting the system has been identified. This phase lag is caused by eddy currents. Two solutions have been proposed, either limit the intensity of the eddy currents by laminating the mover of the actuator or implement flux feedback to compensate for the effects of the eddy current [11]. These solutions are not implemented in this work and are left for future work.

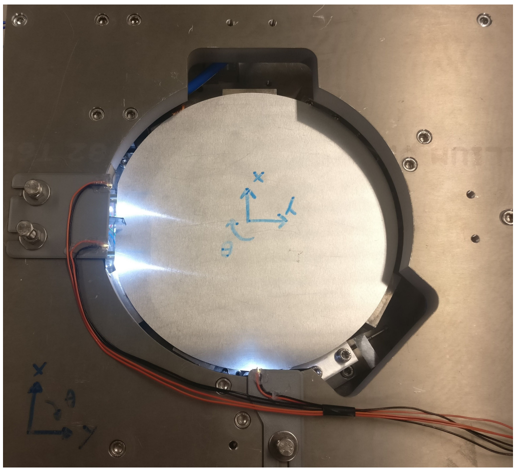

Figure 2: The contactless sensing system implemented in the air-bearing based precision wafer positioning system

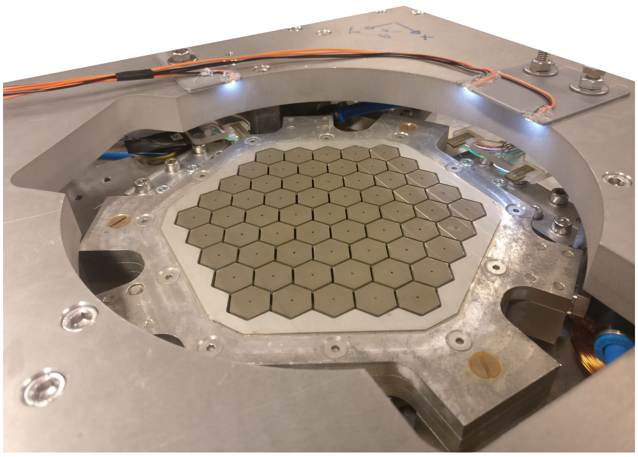

Figure 3: The implemented contactless sensing system without the wafer.

For the outer loop controller a linear charge-coupled device has been implemented as a contactless sensor, shown in Figure 2 and 3. The performance of the sensing system is analyzed. The sensors have a range of 8 mm, with a resolution of 5.5 μm. The steady-state error of the substrate was found to be 12.9 μm RMS, a little more then two times the resolution. The Tracking error was found to be 8.9 mum RMS for motion with range of 0.6 mm. The bandwidth of OLC is approaching 10 Hz. The rotational controller is implemented to prevent rotation.

Contents

1
Introduction

In the high tech industry products such as displays, solar panels and chips are produced. These products are made out of brittle materials for which the thickness is an important factor for the total material costs. Also, the efficiency of the production process can be increased by increasing the size of the substrates. Thereby creating a trend where the substrates increased in size while decreasing in thickness [1]. However, this trend came to a halt due to the percentage of damaged and broken wafers during the manufacturing process.

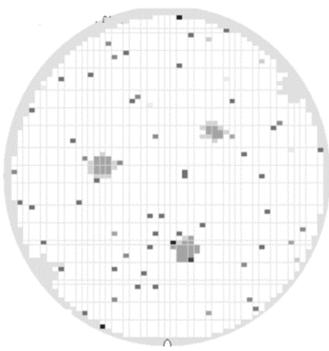

Figure 1.1: Contamination on a wafer due to the wafer supporting pins that are used in wafer handling [2]

The solution is to handle the products without mechanical contact, floating the substrate on a layer of air. This type of air-based levitation is known from air bearing technology, where pressurized air forms a thin air film that separates the two surfaces. This concept eliminates mechanical contact, where friction, backlash, and wear have to be minimized. Furthermore, the layer of air can support the whole surface of the substrate. This is an improvement over the point contact that is currently being used, as air bearings limit contamination and forces on the substrate. This will increase the yield from a single wafer.

Research at the Delft University of Technology shows multiple concepts where substrates are controlled using a thin film flow. The concepts vary in the way the air is controlled, variations of the pressure inlet [4], deformation of the surface to control the airflow [5] and variation of the outlet restriction [10]. This technology has also been used to levitate and transport different kinds of materials, [7] and [8], as the air-based levitation is not limited to certain material properties.

When the substrate is floating it is necessary to measure its position. In the research cited above, the substrates were modified to measure its position. For example, gratings were added to the wafers. Research has been done on contactless positioning, [7] and [9], but systems that do not require any modifications to the substrate have been limited in either bandwidth or resolution.

This thesis presents the air-bearing positioning system with no modifications made to the substrate, in line with how such an air-bearing motion system is to be used in the high-tech industry. The implementations of charge-coupled devices (CCD) is proposed for noncontact position measurement. The sensing concept is implemented in the contactless actuation system and the results are presented.

2

State of the Art

In 2007, Wesselingh started with this new principle of contactless actuation [4]. This concept is used as the basis in the research at the Delft University of Technology for air-based contactless actuation, leading to multiple concepts.

The concepts use the same physics to control the position of the substrate. First, the substrate is levitated on a layer of air. Subsequently, the substrate is preloaded in the out of plane direction with a controlled vacuum source. This increases the out of plane stiffness, at the fly height. This height can be adjusted by changing the force the vacuum and pressure source are applying.

The in-plane actuation is achieved creating an airflow alongside the substrate. The air is flowing from the high-pressure area to the lower pressure following the path of the least resistance. This flow of air exerts a viscous traction force on the substrate. This innovative idea leads to multiple concepts that will be discussed in this section.

2.1. Variable Inlet Pressure

In 2007, Wesseling designed a contactless positioning system based on a fixed geometry and a variable inlet pressure to control the thin film airflow. in his PhD thesis "Contactless Positioning Using an Active Air-Film" [4]. Figure 2.1.a shows a cross-section of one of the actuator cells, where a substrate is floating on top of the pressurized air.

The air will flow from the inlet p+ with high pressure to the outlet p-, where the air is sucked out of the cell. The viscous shear of the airflow creates a traction force on the substrate. The direction of the flow within a cell is controlled by changing the pressure at the inlets. Four actuator cells have to work together to actuate the substrate in three degrees of freedom. The flow of the different cells is separated by dams. Four actuator cells are shown in Figure 2.1.b. The main sensing system is based on edge detection using charge-coupled devices.

The final system was used to position a 4-inch silicon wafer, a demonstrator is shown in Figure2.1.c. A bandwidth of 50 Hz was realized using a PID Controller. The system had a maximum acceleration of 600 mm/s^2, with an error of 6 nm (1σ), while using an external active vibration isolation system. The concept was limited by the manufacturability of the system, as this limited the fly height to 15 μm. A lower fly height would result in a higher actuation force. The other limiting factor is the time delay caused by the pressure lines between the control valve and the pressure inlet in the cell.

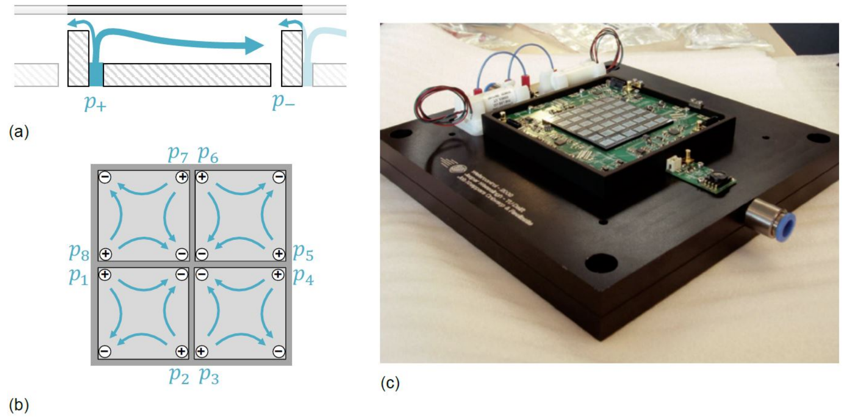

Figure 2.1: Working principle of the first generation. a) Shows the cross-section of an actuator cell. b) Top view. c) The pressure variation demonstrator. [3],[4]

2.2. Variable Outlet Pressure

In 2017, Verbruggen designed the third generation of the contactless actuator which uses an outlet restriction to create the traction force. Figure 2.2, shows the concept in a systematic way. The dams can be actuated to restrict the flow at one side, while the flow is opened up at the other side. The concept is similar to the Variable Inlet pressure design. The advantage of this system is that the restriction is close to the chamber. This is an improvement, as there is no delay present at the supply lines, which limited the Inlet pressure stage.

A demonstrator was built to prove the concept. Seven circular pockets have been produced as shown in Figure 2.2. The substrate was controlled in open loop. Using feedforward average angular accelerations have been measured of 11 rad/s^2.

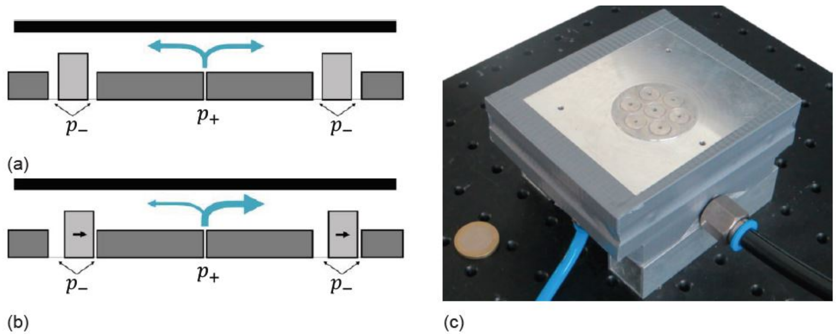

Figure 2.2: The third generation of contactless actuators. a) Schematic of the actuator performing bearing function. b) As used for actuation. c) Shows the demonstrator. [3][10]

2.3. Transportation

Besides positioning a substrate on a stage, this technology could also be used for transportation as this would limit the need for mechanical contact even further. In 2016, Vagher investigated the construction of a passive contactless conveyor [7]. In this research, a cost-effective manufacturing technique for the passive conveyor surface was explored.

Vagher's conveyor concept moves substrates in 1D and measured the position of the substrate using vision. The vision system resulted in a resolution of 30 μm at 60 Hz. Snieder investigated the transition between active and passive surfaces, which makes the transportation concept more versatile [8]. Figure 2.3 shows an example of a transportation system using a combination of passive and active surfaces to transport a substrate.

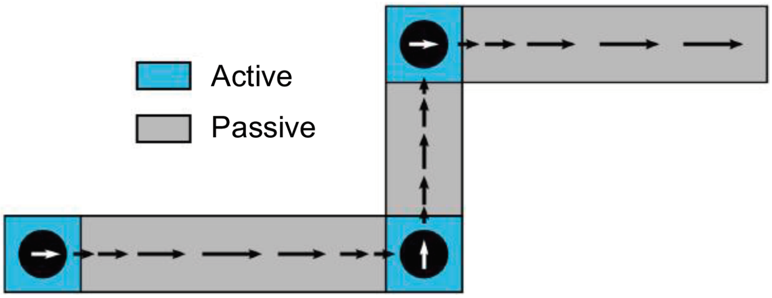

Figure 2.3: An example of transportation using passive and active surfaces. [8]

2.4. Deformable surface

In 2011, Vuong explored a new concept regarding contactless positioning, "Air-based contactless actuation system for thin substrates" [5]". The concept is based on multiple deformable surfaces to steer the airflow, and therefore the force on the substrate. The advantage of the deformable surface is that a change in the geometry directly generates a shear force on the substrate. This concept does not suffer from the delay between the controlling action and force as seen in the first generation. In this concept, the in- and outlet pressure are kept constant. Figure 2.4, shows the titled motion because the shafts are tilted. This concept is used in this paper for precision contactless positioning of the wafer and is explained in detail in the next section.

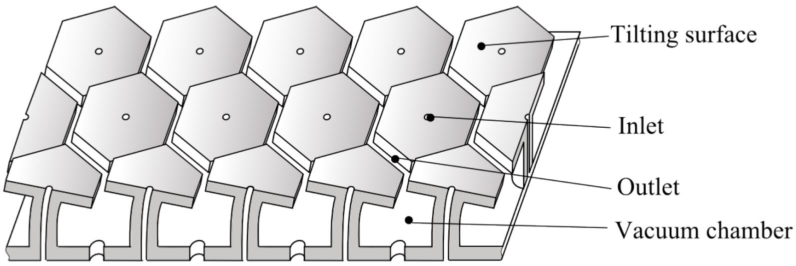

Figure 2.4: The second generation concept, using deformable surfaces. [5]

3
Flowerbed

A demonstrator was built based on the bendable shaft concept. However, instead of bendable shafts, two membranes are used which allows the shafts to tilt. This reduces the force requirement of the actuator. The concept is shown in Figure 3.1. The top membranes are connecting the flowers to the world. The bottom membranes are attached to the movable plate, which is connected to an actuator. The top membranes also function as a seal for the upper chamber, which is connected to the pressure outlet. The inlet pressure comes in through the middle of the shafts.

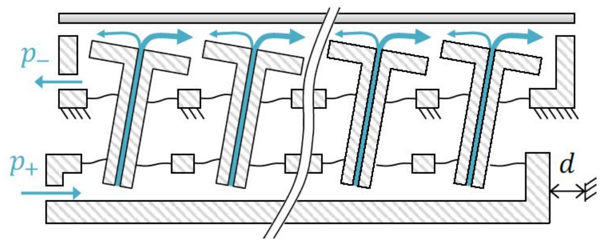

Figure 3.1: Schematic of the second generation contactless actuator, showing the flow of air through the system, for a displacement d of the movable plate. [3]

Figure 3.2 shows a cut-through view of the Flowerbed. The flowerbed has 61 hexagonal heads, with an in-radius of 14 mm. It is nicknamed the Flowerbed because the surface looks like flowers that tilt towards the sun. The hexagon shape is chosen for the flowers because they provide the best packing for a given area and hence provide maximum force for a given airflow. Furthermore, the figure also shows the fixed plate and movable plate. Which both consist of two plates that are clamped together with a 50 μm thick membrane in between. The membrane is also clamped in the flowers. To better align the flowers, the movable plate is preloaded downwards with three springs, with a force of approximately 100 Newton. At last, the flowers were spark eroded to further level the surface, this was done with wire-cut EDM technology.

Figure 3.3 shows a single flower in a neutral and actuated position. The thin film airflow is visualized in the area between the effective surface of the flower and the substrate. In the neutral position, the combination of the positive and negative pressure provides stiffness in the out of plane direction at the fly-height h.

The flowers are tilted with an angle α, through a displacement of the movable plate, as shown in equation 3.1. Where d_p is the displacement of the movable plate and L the distance between the movable plate and the fixed plate.

$$sin(\alpha) = \frac{d_p}{L} \approx \alpha \tag{3.1}$$

When tilted the air will follow the path of least resistance. This flow will, in turn, exert a viscous traction force F_w on the wafer as an addition to the out of plane stiffness.

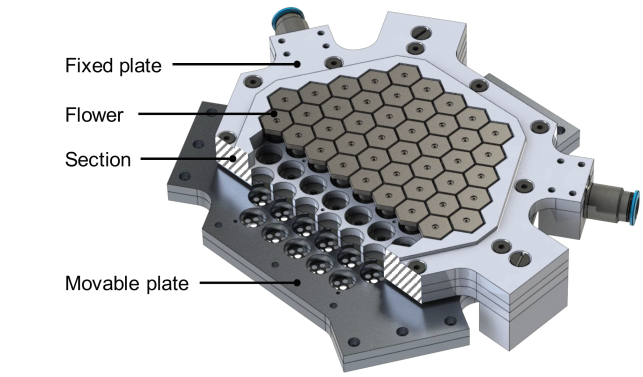

Figure 3.2: A cross-section of the Flowerbed, showing the fixed plate, flowers and movable plate. source: [3]

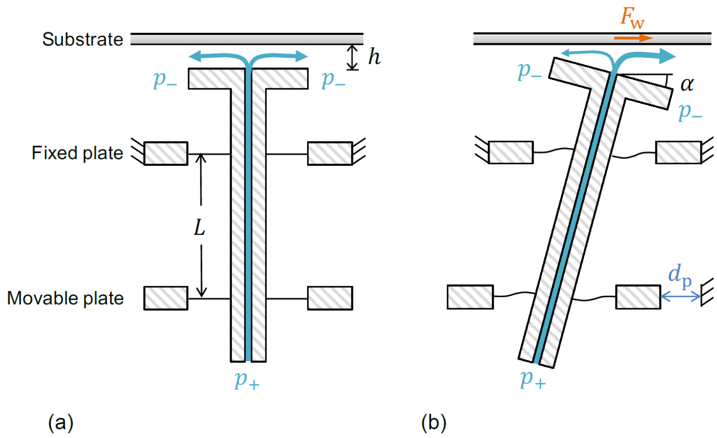

Figure 3.3: Showing a flower of the flowerbed in a) neutral position. b) actuated position. The force on the wafer is visualized in the actuated position. [3]

The tilting angle of the flower is proportional to the displacement of the movable plate up to 1000 Hz, without delay. The tilt response between the flowers is similar, there is only a small deviation in the gain. The values of gain variate between 71 rad/m to 80 rad/m, with the predicted value of 77 rad/m [5]. Furthermore, Vuong experimentally validated that the pneumatics can be modeled by a proportional gain, up to at least 400 Hz. This means that if the movable plate position is known, the force exerted on the wafer is known.

The stiffness of the flowerbed is differs for the translation and rotation of the movable plate. Each flower has a hinge at the top and bottom, which provides stiffness against rotation. Figure 3.4 shows the behavior of the Flowerbed during the translation and rotation of the movable plate. The difference in stiffness results in the suspension eigenmode for the translation and the rotational eigenmode on the rotational stiffness. The numbers have been calculated and experimentally validated by Jansen [3]. The important properties are summarized in Table 3.1.

Table 3.1: Flowerbed Properties

Property		Value
Translational Stiffness	k_{eq}	200 kN/m
Rotational Stiffness	k_θ	2.1 kNm/rad
Equivalent mass	m_{eq}	1.9 kg
Equivallent inertia	I_{eq}	$5.2 \cdot 10^{-3}$ $kg\ m^2$
Translational eigenmode	$f_{0,d}$	51.6 Hz
Rotational eigenmode	$f_{0,\theta}$	101 Hz

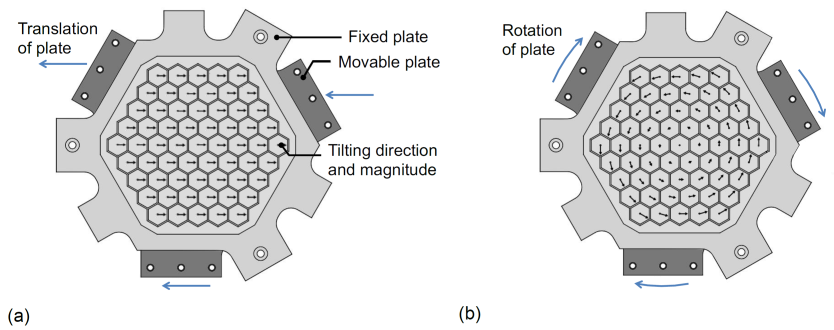

Figure 3.4: Schematic of the flowerbed during a) Translation. b) Rotation. [3].

3.1. Flowerbed Actuation

In 2016, Krijnen designed a Reluctance actuator to actuate the movable plate [6]. Reluctance actuators can provide a high force, but they also have a high mass. With the use of fractional control, this resulted in a control bandwidth for the flowerbed of 100 Hz. The bandwidth was limited by the eigenmodes caused by the actuator as shown in Figure 3.5. Figure 3.6 shows the flapping mode of the actuators that was limiting the bandwidth. The position of the wafer is measured using optical sensors. This required gratings that are attached to the wafer. The position of the wafer is controlled with a bandwidth of 60 Hz.

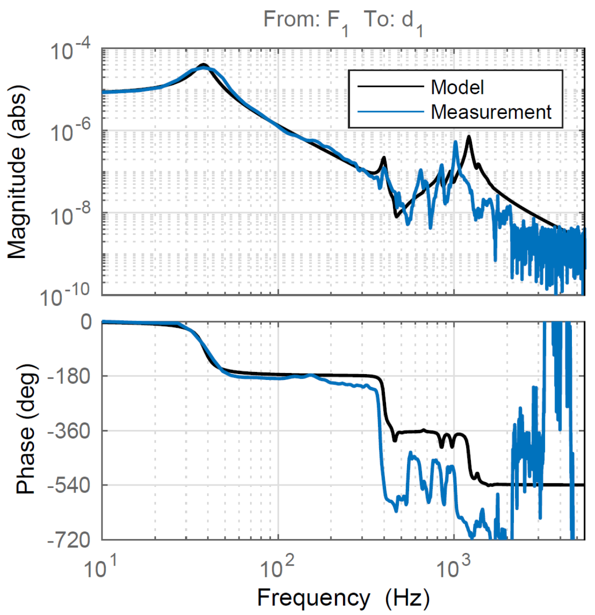

Figure 3.5: The simulated and measured transfer function of the flowerbed with the reluctance actuator. [6].

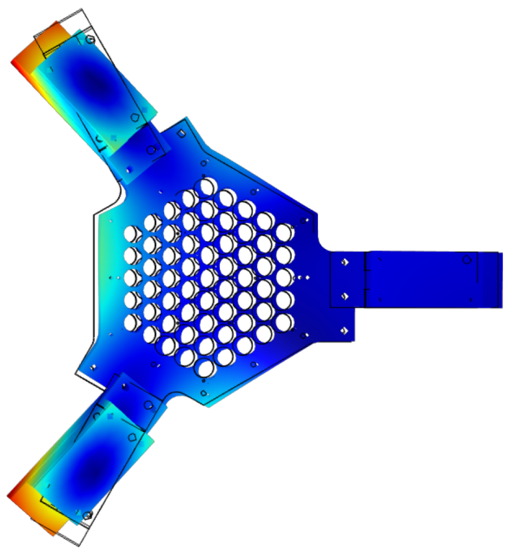

Figure 3.6: Flapping modeshape of the actuators at 1080 Hz (measured). [6].

To increase the bandwidth of the system, Jansen redesigned the actuator in 2018. The new actuator is designed with special care for the dynamic performance. Instead of traditional hinges, a design with notch flexures is chosen. The flexures provide a high stiffness in the out of the plane direction and work without backlash. The reluctance actuators are replaced with Lorentz actuators, as they have a linear force current relation. Furthermore the coil is placed inside the mover such that the mass is kept as low as possible.

Figure 3.7 shows the chosen guidance for the movable plate. In the figure, the application point of the force and sensor are shown, as well as the notch flexure and guide linkages. The sensors that measure the actuator displacement are placed close to the actuator.

Figure 3.8 shows the Flowerbed including the build actuator. From top to bottom it shows the connection between the actuator and movable plate. The coil is used to generate the force on the movable plate. The

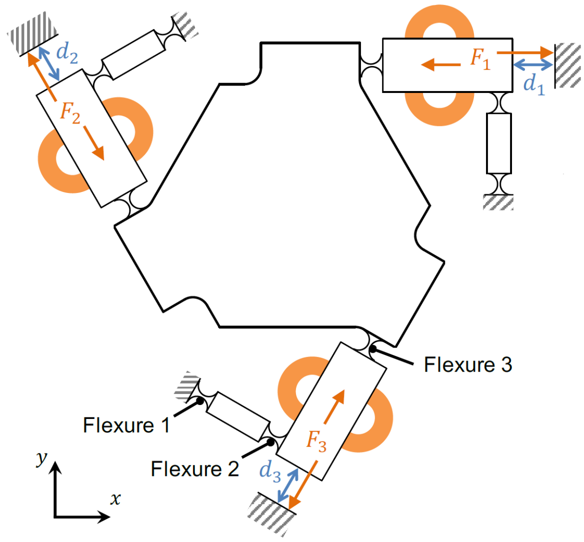

Figure 3.7: Compliant design used to house the actuator. Adapted from [3]

sensor is placed directly behind the actuator. The actuators have a relatively small motion range thus the wires running from the coil to the base plane are no problem. Furthermore, the stiffness is small compared to the stiffness of the movable plate [3].

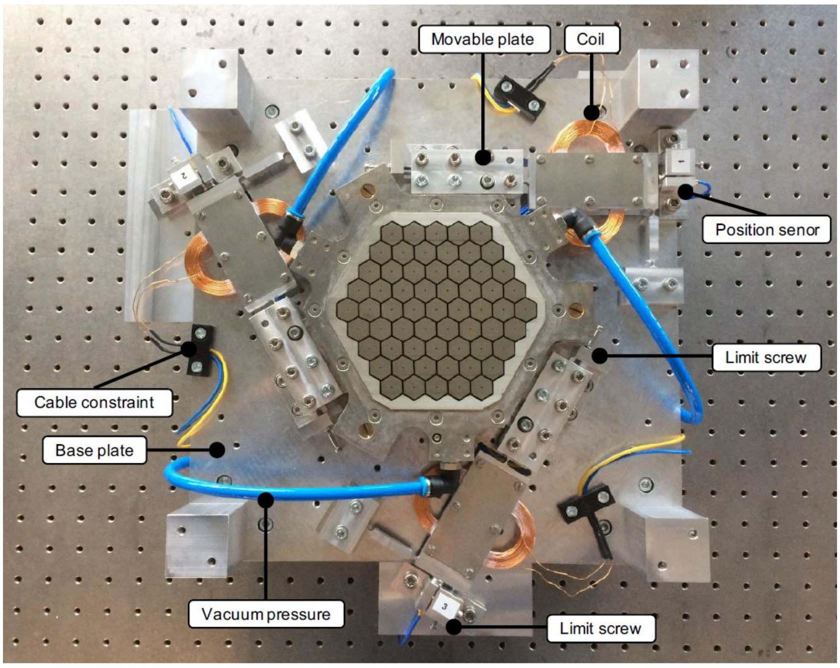

Figure 3.8: Compliant actuator design. [3]

The position of the actuators is measured using Micro-Epsilon CapaNCDT CS08 capacitive sensors, which have a range of 800 μm. With the 16 bits ADC this resulted in a resolution of 24.4 nm. The noise is measured at 0.6 μm Peak-to-peak, with an RMS value of 72 nm.

The redesign of the actuator resulted in a controller with a bandwidth of 233 Hz. The wafer has been controlled in open loop, but no sensing system was implemented to measure its position.

4

Flowerbed Dynamics

In this chapter, the dynamics are experimentally validated. The first step is to identify the system from input force to displacement.

4.1. System Identification

Figure 4.1, shows the results from the identification where all the straight transfers and cross transfers are plotted. Both transfers show a quick drop in phase which is the limiting factor for the bandwidth. Jansen suggested this could be the effect of the capacitive sensing system [3]. In this section, the delay sources are identified.

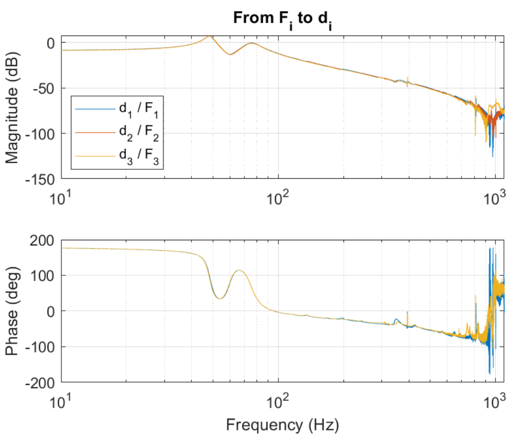

Figure 4.1: Transfer function from actuator Force to actuator displacement, the phase is shifted upwards by 180 degrees.

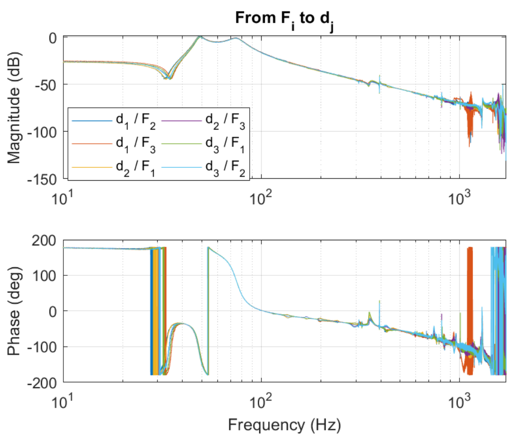

Figure 4.2: The cross-transfers of the flowerbed, the phase is shifted upwards by 180 degrees.

4.1.1. Capacitive Sensors

The specifications of the capacitive sensors are investigated, it is found that the capacitive sensors have a bandwidth of 5 kHz. Since it is used below 1 kHz, the bandwidth does not influence the measurements.

4.1.2. Analog to Digital Convertor

The 16-bits ADC, NI9212, is used within the specified limits as it is rated to 100 thousand samples/s per channel. During the identification and control, it is used at 20 thousand samples/s.

4.1.3. Current Amplifier

The response from the current amplifier is measured, this is shown in Figure 4.3. The bode plot shows a drop in phase, which is caused by the sampling time of 50 μs. The delay of the actuator is within 2 degrees at 500 Hz.

4.1.4. Eddy Currents

Furthermore, the effect of eddy currents is investigated, as the eddy currents in the mover will create a magnetic field opposing the movement. When the magnetic field of the coil and the eddy current is added up, the combined field lags the field of just the coil. The delay of the magnetic field is measured by placing a coil inside the magnetic field. The induced voltage is measured and should lead the current in the coil by 90 degrees as shown in Equation 4.1. Where N is the number of turns in the coil, L the inductance and I the current. The subscript s is used for the measuring coil and p is used for the actuated coil.

$$U_s(s) = s(L\frac{N_p}{Ns})I_p(s) \tag{4.1}$$

Figure 4.4 shows the transfer function from the actuator current to the induced voltage. The figure clearly shows a delay in the phase. The dips around 50 and 70 are related to the resonances in the flowerbed. At the resonance, the movement is bigger and more eddy currents are created, which causes a bigger lag in the magnetic field.

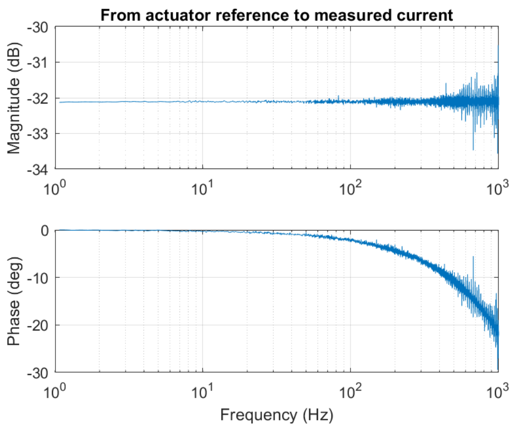

Figure 4.3: Transfer function from actuator set point to the measured current.

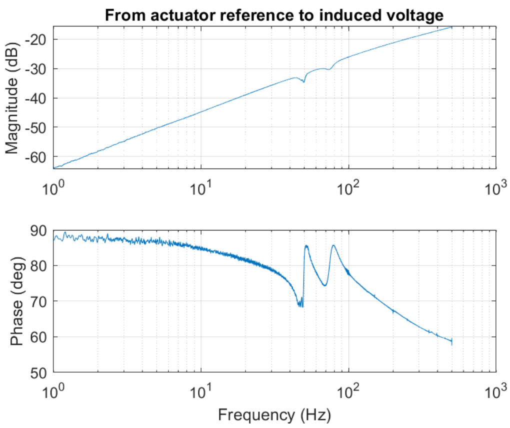

Figure 4.4: Transfer function for the actuator reference to the induced voltage placed in the magnetic field.

Concluding, The phase lag seen in the identification of the plant is mainly due to a combination of the 20 kHz sampling and the effects of the eddy currents.

5

Air-based Contactless Wafer Positioning System, Contactless Sensing Using Charge Coupled Devices

This chapter is presented in a scientific paper format. The work presented in this thesis is summarized in Chapters I to III. In Chapter IV, the dynamic behavior of the flowerbed is discussed and a controller is realized. The implementation of a charge-coupled device (CCD) is proposed for contactless position measurement in Chapter V. The sensing concept is implemented in the contactless actuation system and the results are presented in chapter VI.

Air-based Contactless Wafer Precision Positioning System, Contactless Sensing Using Charge Coupled Devices

R. Hooijschuur, *Precision and Microsystems Engineering*
Delft University of Technology, 2019

***Abstract*—This paper presents the development of a contactless sensing system and the dynamic evaluation of an air-bearing based precision wafer positioning system. The contactless positioning stage is a response to the trend seen in the high-tech industry, where the substrates became thinner and larger to reduce the cost and increase the yield. Using contactless handling it is possible to avoid damage and contamination. The system works by floating the substrate on a thin film of air. A viscous traction force is created on the substrate by steering the airflow.**

A cascaded control design structure has been implemented to the contactless positioning system, where the Inner Loop Controller (ILC) controls the actuator which steers the airflow and the Outer Loop Controller (OLC) controls the position of the substrate by controlling the reference of the ILC.

The dynamics of the ILC are evaluated and optimized for the performance of the positioning of the substrate. The vibration disturbances are also handled by the ILC. The bandwidth of the system has been improved to 300 Hz.

For the OLC a linear charge-coupled device has been implemented as a contactless sensor. The performance of the sensing system has been analyzed. During control in steady state, this resulted in a position error of the substrate of 12.9 μm RMS, which is a little more as two times the resolution. The bandwidth of OLC is approaching 10 Hz.

I. Introduction

In the high tech industry products such as displays, solar panels and chips are produced. These products are made out of brittle materials where the thickness is an important factor. The thickness of the raw material is a factor in the total material costs. Also, the efficiency of the production process can be increased by increasing the size of the substrates. This is why there was a trend where the substrates increased in size while decreasing in thickness [1]. However, this trend came to a halt due to the percentage of damaged and broken wafers during the manufacturing process.

The solution is to handle the products without mechanical contact, floating the substrate on a layer of air. This type of air-based levitation is known from air bearing technology, where pressurized air forms a thin air film that separates the two surfaces. This concept is an alternative to mechanical contact, where friction, backlash, and wear have to be minimized. Furthermore, the layer of air can support the whole surface of the substrate. This is an improvement over the point contact that is currently being used [2], as air bearing limits contamination and forces on the substrate. This will increase the yield from a single wafer.

Research at the Delft University of Technology shows multiple concepts where substrates are controlled on a controlled layer of air. The concepts vary in the way the air is controlled, variations of the pressure inlet [4], deformation of the surface to control the airflow [5] and variation of the outlet restriction [10]. This technology has also been used to levitate and transport different kinds of materials, [7] and [8], as the air-based levitation is not limited to certain material properties.

When the substrate is floating it is necessary to measure its position. In the research cited above, the substrates were modified to measure its position. For example, gratings were added to the wafers. Research has been done on contactless positioning, [7] and [9], but sensing systems that do not require any modifications to the substrate have been limited in either bandwidth or resolution.

This paper presents the first air-bearing positioning system where no modifications are made to the substrate, in line with how such an air-bearing motion system is to be used in the high-tech industry. The implementations of a charge-coupled device (CCD) is proposed for noncontact position measurement. The sensing concept is implemented in the contactless actuation system and the results are presented.

In section II, the state of the art is presented. Section III explains the contactless actuation concept based on deformable surfaces. The dynamics response of the actuator is evaluated and a controller is designed, in section IV. Section V shows the proposed sensor concept with performance analysis. The sensor is implemented in the contactless actuation system and the results are presented in Section VI.

II. State of the Art

In 2007, Wesselingh started with this new principle of contactless actuation [4]. This concept is used as the basis in the research at the Delft University of Technology for air-based contactless actuation, which let to multiple concepts.

The concepts use the same physics to control the position of the substrate. First, the substrate is levitated on a layer of air. Subsequently, the substrate is preloaded in the out of plane direction with a controlled vacuum source. This increases the out of plane stiffness, at the fly height. This height can be adjusted by changing the force the vacuum and pressure source are applying.

The in-plane actuation is achieved creating an airflow alongside the substrate. The air is flowing from the high-pressure area to the lower pressure following the path of the least resistance. This flow of air exerts a viscous traction force on the substrate. This innovative idea leads to multiple concepts that will be discussed in this section.

A. Variable Inlet Pressure

In 2007, Wesseling designed a contactless positioning system based on a fixed geometry and a variable inlet pressure to control the thin film airflow. in his PhD thesis "Contactless Positioning Using an Active Air-Film" [4]. Figure 1.a shows a cross-section of one of the actuator cells, where a substrate is floating on top of the pressurized air.

The air will flow from the inlet p+ with high pressure to the outlet p-, where the air is sucked out of the cell. The viscous shear of the airflow creates a traction force on the substrate. The direction of the flow within a cell is controlled by changing the pressure at the inlets. Four actuator cells have to work together to actuate the substrate in three degrees of freedom. The flow of the different cells is separated by dams. Four actuator cells are shown in Figure 1.b. The main sensing system is based on edge detection using charge-coupled devices.

The final system was used to position a 4-inch silicon wafer, a demonstrator is shown in Figure1.c. A bandwidth of 50 Hz was realized using a PID Controller. The system had a maximum acceleration of 600 mm/s^2, with an error of 6 nm (1σ), while using an external active vibration isolation system. The concept was limited by the manufacturability of the system, as this limited the fly height to 15 μm. A lower fly height would result in a higher actuation force. The other limiting factor is the time delay caused by the pressure lines between the control valve and the pressure inlet in the cell.

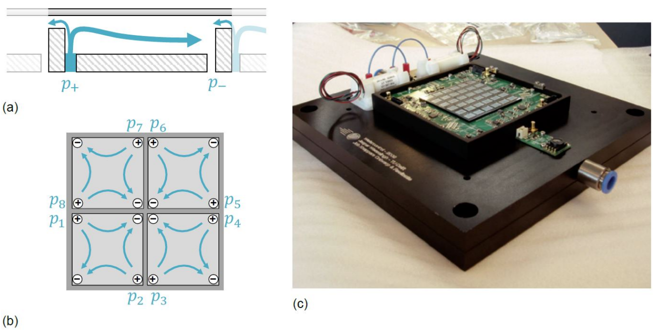

Fig. 1. Working principle of the first generation. a) shows the cross-section of an actuator cell. b) top view. c) The pressure variation demonstrator. [3], [4]

B. Variable Outlet Restriction

In 2017, Verbruggen designed the third generation of the contactless actuator which uses an outlet restriction to create the traction force. The dams can be actuated to restrict the flow at one side, while the flow is opened up at the other side. The concept is similar to the Variable Inlet pressure design. The advantage of this system is that the restriction is close to the chamber. This is an improvement, as there is no delay present at the supply lines, which limited the Inlet pressure stage.

A demonstrator was built to prove the concept. Seven circular pockets have been produced. The substrate was controlled in open loop. Using feedforward average angular accelerations have been measured of 11 rad/s^2.

C. Transportation

Besides positioning a substrate on a stage, this technology could also be used for transportation as this would limit the need for mechanical contact even further. In 2016, Vagher investigated the construction of a passive contactless conveyor [7]. In this research, a cost-effective manufacturing technique for the passive conveyor surface was explored.

Vagher's conveyor concept moves substrates in 1D and measured the position of the substrate using vision. The vision system resulted in a resolution of 30 μm at 60 Hz. Snieder investigated the transition between active and passive surfaces, which makes the transportation concept more versatile [8].

D. Deformable surface

In 2011, Vuong explored a new concept regarding contactless positioning, "Air-based contactless actuation system for thin substrates" [5]. The concept is based on multiple deformable surfaces to steer the airflow, and therefore the force on the substrate. The advantage of the deformable surface is that a change in the geometry directly generates a shear force on the substrate. This concept does not suffer from the delay between the controlling action and force as seen in the first generation. In this concept, the in- and outlet pressure are kept constant. The concept were the surfaces are tilted by bending the shafts is shown in Figure 2. This concept is used in this paper for precision contactless positioning of the wafer and is explained in detail in the next section.

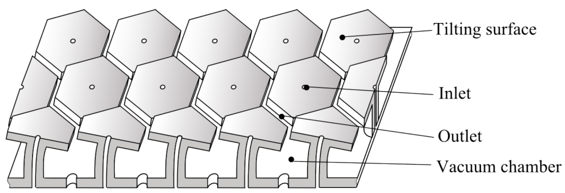

Fig. 2. The deformable surface concept, The surfaces are titled by bending the shafts. [5]

III. FLOWERBED

A demonstrator was built based on the bendable shaft concept. However, instead of bendable shafts, two membranes are used which allows the shafts to tilt. This reduces the force requirement of the actuator. The concept is shown in Figure 3. The top membranes are connecting the flowers to the world. The bottom membranes are attached to the movable plate, which is connected to an actuator. The top membranes also function as a seal for the upper chamber, which is connected to the pressure outlet. The inlet pressure comes in through the middle of the shafts.

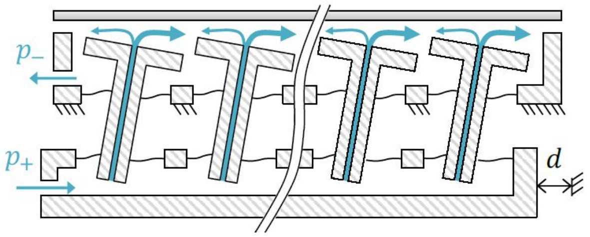

Fig. 3. Schematic of the second generation contactless actuator, showing the flow of air through the system, for a displacement d of the movable plate. [3]

Figure 4, shows a cut-through view of the Flowerbed. The flowerbed has 61 hexagonal heads, with an in-radius of 14 mm. It is nicknamed the Flowerbed because the surface looks like flowers that tilt towards the sun. The hexagon shape is chosen for the flowers because they provide the best packing for a given area and hence provide maximum force for a given airflow. Furthermore, the figure also shows the fixed plate and movable plate. Which both consist of two plates that are clamped together with a 50 μm thick membrane in between. The membrane is also clamped in the flowers. To better align the flowers, the movable plate is preloaded downwards with three springs, with a force of approximately 100 Newtons. At last, the flowers were spark eroded to further level the surface, this is done with wire-cut EDM technology.

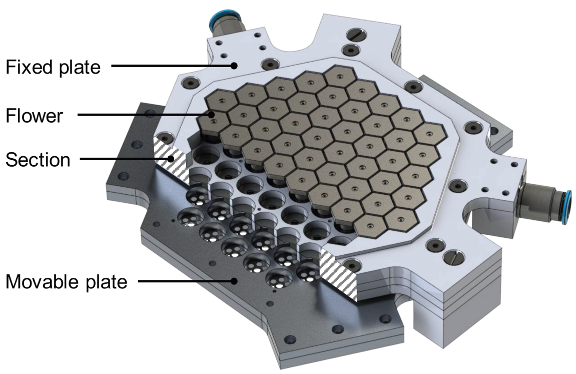

Fig. 4. A cross-section of the Flowerbed, showing the fixed plate, flowers and movable plate. source: [3]

Figure 5, shows a single flower in a neutral and actuated position. The thin film airflow is visualized in the area between the effective surface of the flower and the substrate. In the neutral position, the combination of the positive and negative pressure provides stiffness in the out of plane direction at the fly-height h.

The flowers are tilted with an angle α, through a displacement of the movable plate, as shown in equation 1. Where d_p is the displacement of the movable plate and L the distance between the movable plate and the fixed plate.

$$sin(\alpha) = \frac{d_p}{L} \approx \alpha \tag{1}$$

When tilted the air will follow the path of least resistance. This flow will, in turn, exert a viscous traction force F_w on the wafer as an addition to the out of plane stiffness.

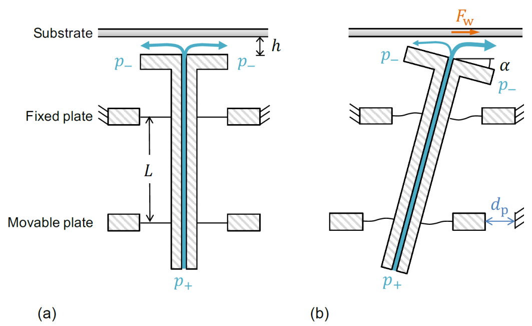

Fig. 5. Showing a flower of the flowerbed in a) neutral position. b) actuated position. The force on the wafer is visualized in the actuated position. [3]

The tilting angle of the flower is proportional to the displacement of the movable plate up to 1000 Hz, without delay. The tilt response between the flowers is similar, there is only a small deviation in the gain. The values of gain variate between the 71 rad/m to 80 rad/m, where the predicted value is 77 rad/m [5]. Furthermore, Vuong experimentally validated that the pneumatics can be modeled by a proportional gain, up to at least 400 Hz. This means that if the movable plate position is known, the force exerted on the wafer is known.

The stiffness of the flowerbed is different for the translation and rotation of the movable plate. Each flower has a hinge at the top and bottom, which provide stiffness against the rotation. Figure 6, shows the behavior of the Flowerbed during the translation and rotation of the movable plate. The difference in stiffness results in the suspension eigenmode for the translation and the rotational eigenmode on the rotational stiffness. The numbers have been calculated and experimentally validated by Jansen [3]. The important properties are summarized in Table I.

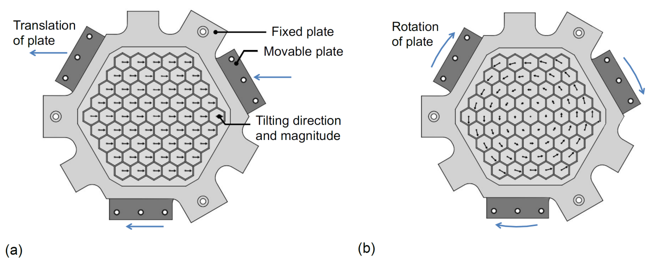

Fig. 6. Schematic of the flowerbed during a) Translation. b) Rotation. [3].

A. *Flowerbed Actuation*

In 2016, Krijnen designed a Reluctance actuator to actuate the movable plate [6]. Reluctance actuators can provide a

TABLE I
FLOWERBED PROPERTIES

Property		Value
Translational Stiffness	k_{eq}	200 kN/m
Rotational Stiffness	k_{θ}	2.1 kNm/rad
Equivalent mass	m_{eq}	1.9 kg
Equivallent inertia	I_{eq}	$5.2 \cdot 10^{-3}$ $kg\ m^2$
Translational eigenmode	$f_{0,d}$	51.6 Hz
Rotational eigenmode	$f_{0,\theta}$	101 Hz

high force, but they also have a high mass. With the use of fractional control, this resulted in a control bandwidth for the flowerbed of 100 Hz. The bandwidth was limited by the eigenmodes caused by the actuator as shown in Figure 7. Figure 8, shows the flapping mode of the actuators that was limiting the bandwidth. The position of the wafer is measured using optical sensors. This required that gratings are attached to the wafer. The position of the wafer is controlled with a bandwidth of 60 Hz.

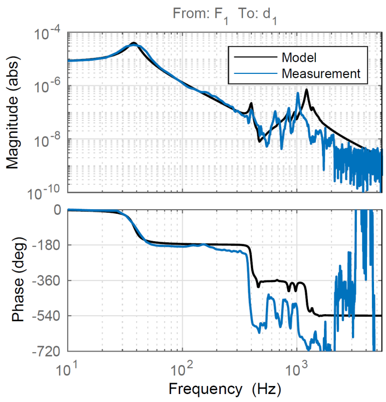

Fig. 7. The simulated and measured transfer function of the flowerbed with the reluctance actuator. [6].

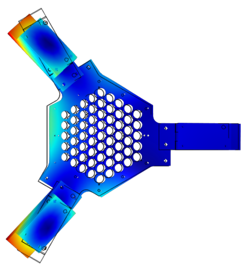

Fig. 8. Flapping modeshape of the actuators at 1080 Hz (measured). [6].

To increase the bandwidth of the system, Jansen redesigned the actuator in 2018. The new actuator is designed with special care for the dynamic performance. Instead of traditional hinges, a design with notch flexures is chosen. The flexures provide a high stiffness in the out of the plane direction and work without backlash. The reluctance actuators are replaced with Lorentz actuators, as they have a linear force current relation. Furthermore the coil inside the mover such that the mass is kept as low as possible.

Figure 9, shows the chosen guidance for the movable plate. In the figure, the application point of the force and sensor are shown, as well as the notch flexure and guide linkages. The sensors that measure the actuator displacement are placed close to the actuator.

Figure 10, shows the Flowerbed including the build actuator. From top to bottom it shows the connection between the actuator and movable plate. The coil is used to generate the force on the movable plate. The sensor is placed directly behind the actuator. The actuators have a relatively small motion range thus the wires running from the coil to the

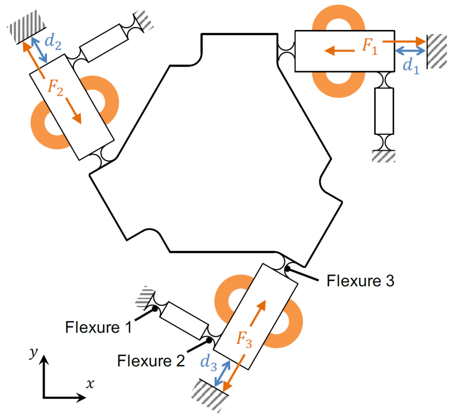

Fig. 9. Compliant design used to house the actuator. Adapted from [3]

base plane are no problem. Furthermore, the stiffness is small compared to the stiffness of the movable plate [3].

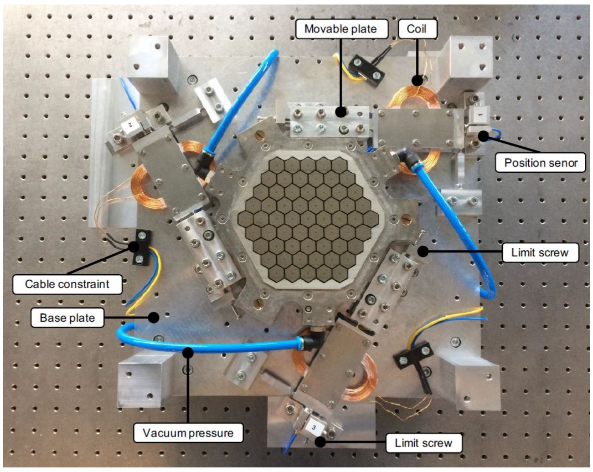

Fig. 10. Compliant actuator design. [3]

The position of the actuators is measured using Micro-Epsilon CapaNCDT CS08 capacitive sensors, which have a range of 800 μm. With the 16 bits ADC this resulted in a resolution of 24.4 nm. The noise is measured at 0.6 μm Peak-to-peak, with an RMS value of 72 nm.

IV. FLOWERBED DYNAMICS AND CONTROL

In the previous sections, the state of the art has been presented. The bandwidth of the compliant actuator design was placed on 233 Hz. No sensor was implemented to measure the position of the wafer. In this section, the dynamic response of the system is presented. A controller is designed and the results are discussed using the closed-loop. At last, the possibilities for improvement are discussed.

A. Flowerbed Dynamics

Figure 11, shows the results from the identification where all the straight transfers and cross transfers are plotted. Both transfers show a quick drop in phase which is the limiting factor for the bandwidth. Jansen suggested this could be the effect of the capacitive sensing system [3]. After investigation of the delay sources in the system; amplifier, capacitive sensors, sampling time, coil dynamics, the main sources of the delay are found. The phase lag is due to a combination of the 20 kHz sampling which produces a phase lag and the magnetic field which is lagging the current. The lagging field is due to the Eddy currents in the mover which will create a magnetic field opposing the movement. When the magnetic field of the coil and eddy current are added up the field lags the field of just the coil. This provides a time delay seen in the bode diagram as a lagging phase. Furthermore, the eddy current damping provides damping of the magnitude based on the velocity of the mover.

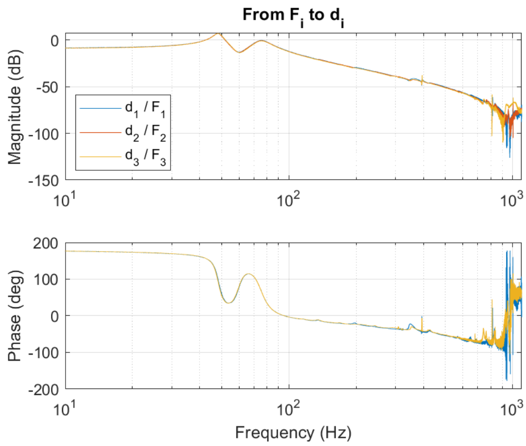

Fig. 11. Transfer function from actuator Force to actuator displacement, the phase is shifted upwards by 180 degrees.

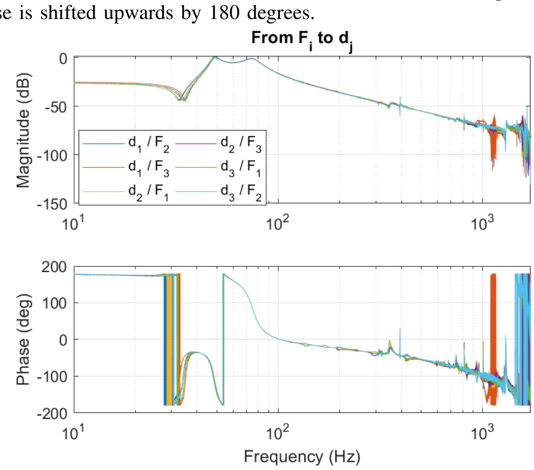

Fig. 12. The cross-transfers of the flowerbed, the phase is shifted upwards by 180 degrees.

Figure 13, shows the mover in the magnetic field of the permanent magnets. The mover consists of an aluminum plate with spaces cut out for the coils and a top plate to hold them in place. A solution to limit the intensity of the eddy currents that are created is to laminate the mover. Another method is to look at the possibility of flux feedback, to compensate for the effects of the eddy current [11]. These solutions are not implemented in this work and are left for future work.

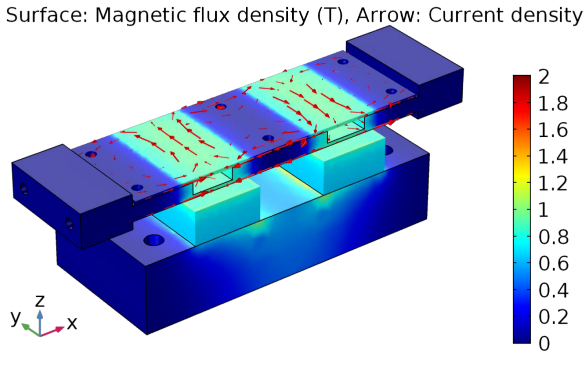

Fig. 13. Eddy currents [3]

B. Flowerbed Control

The controller of the inner loop will control the position of the actuator to the corresponding sensor. The measured position will be controlled using a feedforward controller and Feedback controller. The diagram is shown in Figure 14.

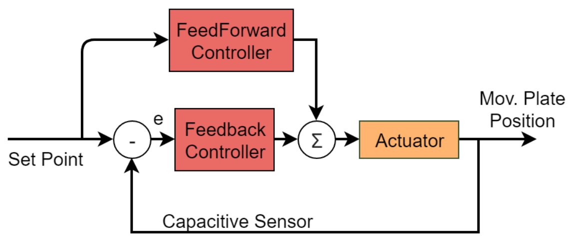

Fig. 14. Movable plate control strategy.

For the feedback controller, a PID controller is designed for a bandwidth of 300 Hz. The parameters are shown in Table II, the gain for actuator 2 is different to compensate for the slightly different stiffness at the bandwidth. The Controller creates a Phase margin of 27 degrees, Gain Margin of 32.7 dB and a Modulus Margin of 11.3 dB.

TABLE II
PID PARAMETERS

Parameter		Actuator 1	Actuator 2	Actuator 3
K	N/m	15.2	14.8	15.2
f_i	Hz	10	10	10
f_d	Hz	50	50	50
f_t	Hz	2000	2000	2000
f_f	Hz	2500	2500	2500

The feedforward controller has been designed using a simplification of the plant. The feedforward controller is the inverse of this plant made proper with with two second-order low pass filters at the frequency of the bandwidth. The closed-loop response of the system with the PID controller and feedforward is shown in Figures 15 and 16. The feedforward controller is given in Equation 2.

$$FF = -\frac{\left(\frac{s}{300}+1\right)\left(\frac{s^2}{(2\pi 49)^2}+\frac{0.1\,s}{2\pi 49}+1\right)}{0.37\left(\frac{s^2}{300^2}+\frac{2\,s}{300}+1\right)^2}\cdot \frac{\left(\frac{s^2}{(2\pi 75)^2}+\frac{0.17\,s}{2\pi 75}+1\right)}{\left(\frac{s^2}{(2\pi 60)^2}+\frac{2\,s}{2\pi 60}+1\right)} \quad (2)$$

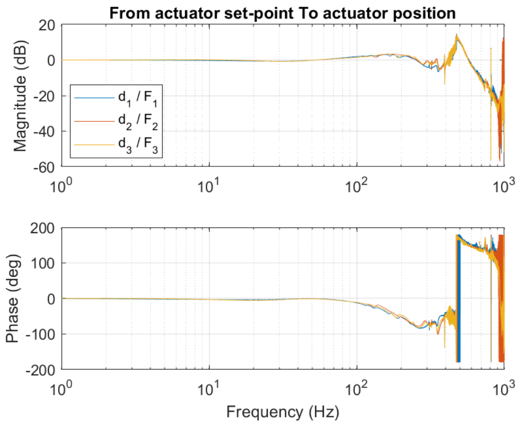

Fig. 15. Closed loop measurement of the actuators, from actuator setpoint to measure position.

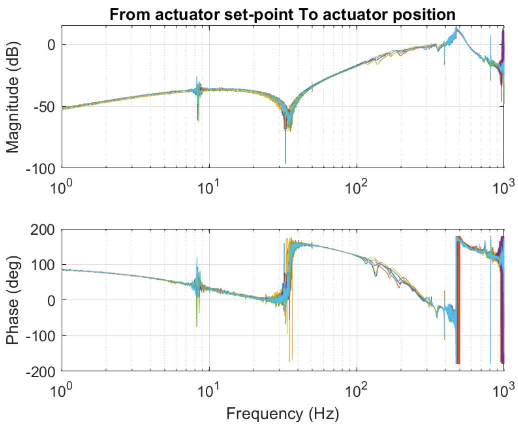

Fig. 16. Closed loop cross transfer measurement of the actuators, from actuator setpoint to measure position.

The closed-loop response of the system is similar for all three actuators. The response provides a good basis for the Outer Loop Controller up to, at least 100 Hz. The system shows strong coupling at 470 Hz, this could be improved using a decoupling filter or by prefiltering the input. Because the bandwidth of the outer loop is limited, it is chosen to use the Outer Loop Controller to prefilter the reference signal.

V. Wafer Sensing

The wafer floating on air is a mass system, thus to gain control over the position of the wafer it is necessary to have a collocated sensor. For this sensor in the outer loop, there are some restrictions, that influence the sensor choice. For the high-tech industry, it is unappealing to use a wafer with big gratings on the surface as this would lower the yield. Thus, it is preferred that the wafer is not altered.

As discussed in the state of the art, different sensor techniques are used in the past. Techniques based on capacitive sensors, edge detection using Charge-Coupled Devices (CCD), vision and optical encoders. The best speed and resolution was achieved using optical encoder with gratings on the wafer. However, this is an alteration to the wafer. Without altering the wafer edge detection using the linear CCD sensor array is the best choice. Edge detection can reach sampling speeds up to multiple kHz while having a sub-micrometer resolution could be achieved using sub-pixel interpolation. This will be discussed later in this section.

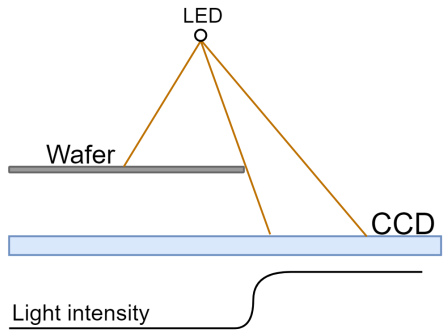

Fig. 17. Linear CCD sensor concept to measure the edge of a wafer

A. Linear Sensor Array

A linear CCD has been selected to measure the position of the wafer. It an array of pixels, that measure the intensity of the light. The change from light to dark is used to find the edge of the wafer. The concept is shown in Figure 17. As discussed in the state of the art, Wesselingh had implemented CCD sensors, but used a different concept were noise from stray light limited the performance [4].

The selection of the CCD sensor is based on a tradeoff between the resolution, sampling time and range. The sampling time is limited by the available modules for the National Instruments CompactRio. The NI9201 is used which supports 500 kS/s. The TCD1103GFG has 1500 pixels of 5.5 μm by 64 μm on 5.5 μm center. It supports a data rate of 2 MHz. With 1500 pixels and a low integration time this results in a sampling rate of almost 1.3 kHz, with the limitation of the 500 kS/s this is lowered to 320 Hz. High power cool white LEDs are used as the light source. The intensity of the light is tuned to maximize the dynamic range.

In this paper, the sensor output is compared to a threshold. This threshold is used to detect the transition from light to dark. Instead of using a threshold a sub-pixel interpolation method could be used. Using this method it is possible to increase the resolution of the sensors to at least 0.05 of the pixel size, while reducing the effects of noise [15], [16], [17], and [18]. Using the sub-pixel interpolation method the theoretic resolution of the chosen CCD could be as low as 0.11 μm. However, to limited the calculation time on the FPGA, it was chosen to implement the threshold model. Figure 20, shows the output of the CCD sensor. The threshold is placed at 0.6. When the threshold is reached the pixel number corresponds to the position on the CCD where the shadow ends.

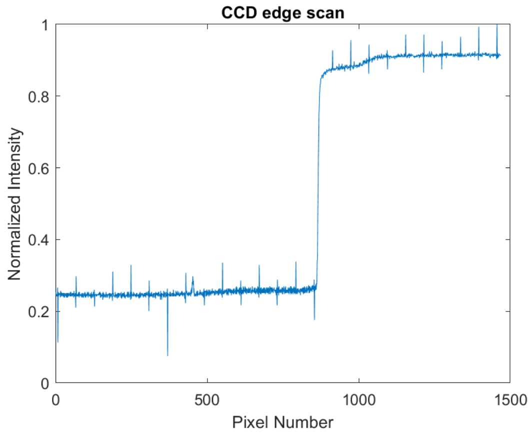

Fig. 18. Output of the CCD sensor. It shows the edge of the wafer. The edge is a curve over 10 pixels.

When using a point light source, the measured position should be adjusted to get the real position. Figure 19, show that distance between the shadow and the wafer position is dependent on the position and height of the wafer. The wafer position is calculated using 3a. Because the height of the wafer is not fixed a disturbance could enter the system through a variation in the height. The size of the disturbance could be estimated by 3a.

The difference in fly-height is estimated to be in the order of micrometers. When minimizing the height between the wafer and CCD the disturbance is estimated to be within 0.1 of the pixel size for large movements, which is acceptable when using the threshold model, if sub-pixel interpolation is used it is better to remove the height by using a collimated light source or adding another LED. With two LEDs another data point is known, which can be used to eliminate the height from the equation as shown in Equation 3b [13].

$$X_w = \frac{h_{wafer}}{h_{led}}(x_{L1} - xs1) + s1 \tag{3a}$$

$$X_w = \frac{x_{L2}x_{s1} - x_{L1}x_{s2}}{-x_{L1} + x_{L2} + x_{s1} - x_{s2}} \tag{3b}$$

B. *Performance Analysis*

Before the implementation of the CCD sensor inside the contactless actuator, a performance analysis experiment was done. In these tests, the linearity of the sensor was tested, as well as the steady-state behavior. The performance test was performed in an environment where sources from the external lighting, vibrations, and the electrical side are not removed. The steady-state response shows no drift and high precision, as the position comes back to the same position. Figure 20, shows the performance analysis test where the position of the CCD is compared to a stage which has a resolution of 100 nm. The figure shows no drift and follows the position of the stage with an error of 3.0 um RMS.

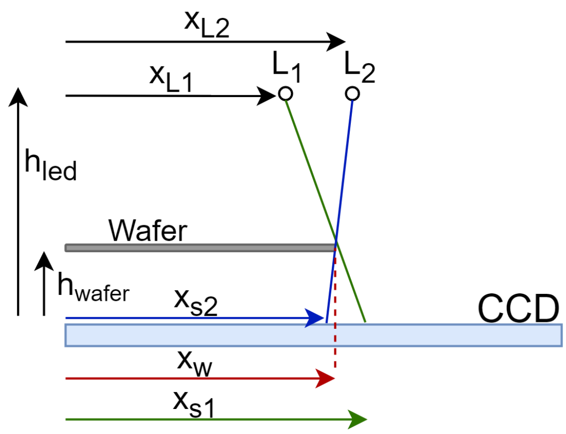

Fig. 19. A CCD sensors with 2 LEDs, showing the actual position of the wafer x_w, the shadow created by the first led x_{s1} and second led x_{s2}
.

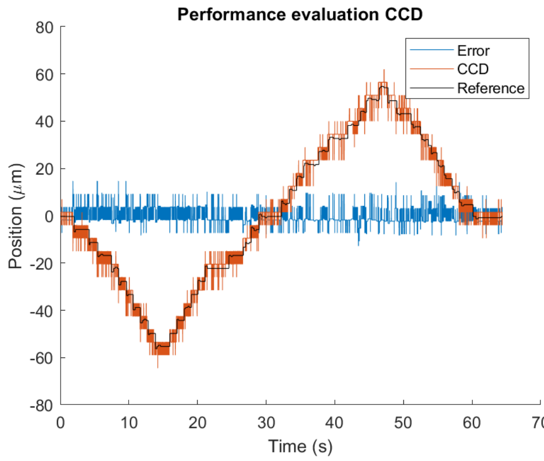

Fig. 20. Shows the response of the CCD sensor RMS value 3.0 μm

C. *Metrology*

The kinematics are used to convert the measured position from the sensors into the position of the wafer. Figure 21, shows the placement of the sensors. The kinematic equations are shown in Equation 4, where r is the radius of the wafer and 41.5 the distance between the sensors. The input of the kinematic equations is in millimeters and the output is in millimeters and radians.

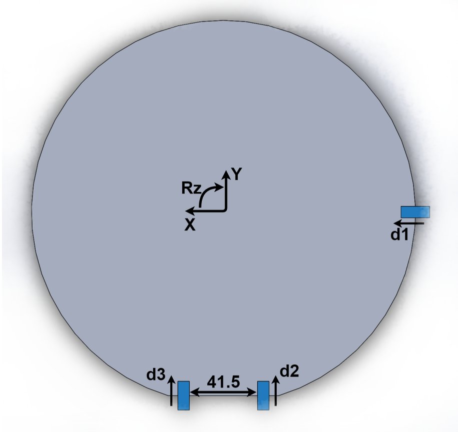

Fig. 21. The raw response of the CCD sensor.

$$y = \frac{d_2 + d_3}{2} \tag{4a}$$

$$x = d_1 + r - \sqrt{r^2 - y^2} \tag{4b}$$

$$Rz = \frac{d_3 - d_2}{41.5} \tag{4c}$$

The measurement in the outer loop performed using a 200 mm dummy wafer. The dummy wafer is cut out of a 750 μm thick aluminum and according to the JEIDA standard [14]. This means a circle with a radius of 100 mm with a flat of 57.5 mm. The aluminum wafer weighs 63 grams, which is 8 percent more as the silicon wafer.

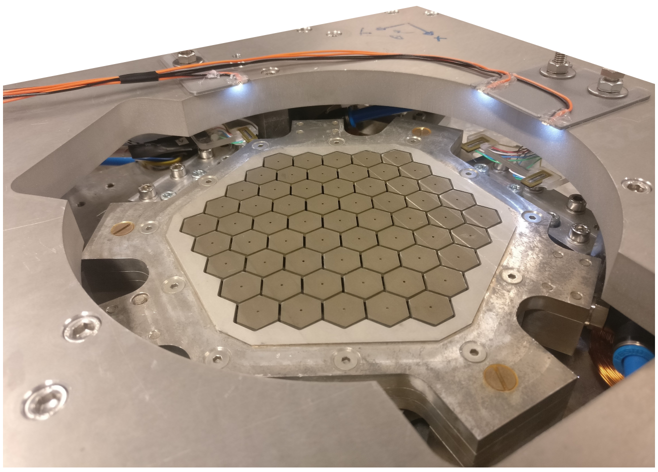

Fig. 22. The implemented contactless sensing system without the wafer.

VI. Wafer Control

To control the position of the wafer, a second controller need to be added to the existing one. This leads to a cascaded control structure as shown in Figure 23. The flowerbed controller will be called the Inner Loop Controller (ILC) from now on. The ILC will provide the stiff connection between the flowerbed and actuator after the suspension resonance frequency. The setpoint of the ILC will be controlled by the wafer controller, which is also called the Outer Loop Controler (OLC). The kinematics and inverse kinematics are placed in the loop of the OLC, because the OLC has a lower bandwidth and thus more time for the calculations.

A. Pressure control

For the operation of the Flowerbed, constant pressure and vacuum are crucial. Even more because of an offset in the pressure chambers. Choosing a higher pressure will cause an extra force in the negative y-direction, where a lower vacuum will create an extra force in the positive y-direction.

TABLE III
Pressure controller properties

Parameter	Pressure	Vacuum
Kp	5000	-1000
f_f	90	150

To control the pressure, sensors and valves are placed in the supply lines. The dynamic behavior of the pressure and vacuum supply has been identified around the operation pressure of 240 kPa supply and 6 kPa vacuum. The controller design is a proportional gain together with a second-order low pass filter. The lower bandwidth has been chosen because of the limitations of the solenoid valves, increasing the bandwidth further does not improve the performance. During control the steady-state error is measured, the error for the vacuum controller is 0.01 kPa (σ) and for the pressure controller 0.3 kPa (σ).

B. Pneumatics

Previous experiments by Vuong showed that the air film dynamics can be described as a proportional gain up to at least 400 Hz, after which the measurement became unreliable [5]. The proportional gain of the system was determined at 1.4 $mN/\mu m$ In short, this means that if the position of the movable plate is known, the viscous traction force on the wafer can be calculated up to at least 400 Hz. This value of the proportional gain is verified during the experiments of Krijnen [6]. Furthermore, Krijnen provided the displacement force graph for different supply pressures while maintaining the vacuum supply at ambient pressure minus 7 kPa.

Multiple experiments are done with the values provided by Krijnen, however with the pneumatic gain could not be reached without contact. Multiple factors play a role here, the flowerbed has been taken apart and reassembled by Jansen to replace the actuators. Upon close inspection, it appears that multiple flowers are out of alignment. Furthermore, the supply pressure is leaking between the pressure sensor and the flowerbed. This makes the sensor readings unreliable. The combination of these factors made that the noncontact criteria could not be guaranteed at the given pressure. Therefore the pressure was manually tuned to obtain the best performance while keeping the no contact condition for a movement 60 μm

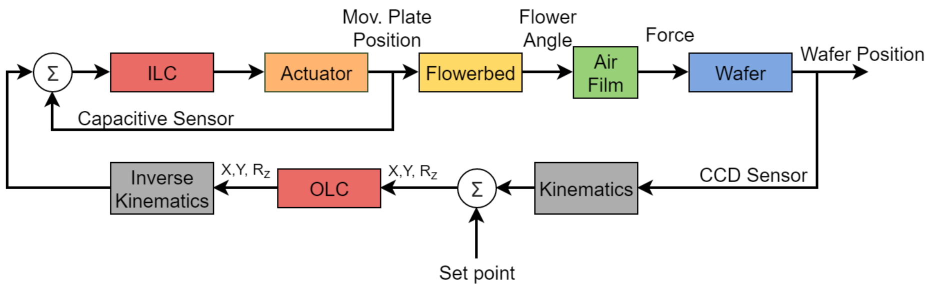

Fig. 23. The control strategy for the flowerbed.

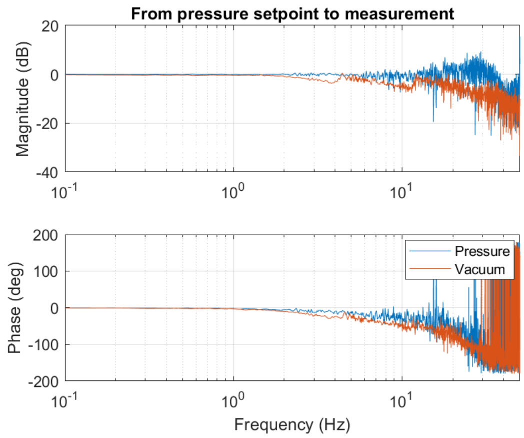

Fig. 24. The control strategy for the flowerbed. [6]

for the movable plate. The optimum was found at the vacuum pressure at minus 6 kPa and supply pressure of 245 kPa. As a result, the value of the pneumatic gain is lowered.

C. *Outer loop controller*

In the outer loop, two controllers have been designed, one for blocking the rotation at lower bandwidth and one for positioning the wafer in x and y to increase the performance of the total system. The parameters of the controller will be discussed later in this section.

The outer loop could not be identified using the open-loop response because the system consists of a floating mass. The identification of the system could be done by adding stiffness to the mass or through simulation. The open-loop could be described by the transmissibility of the inner loop controller (T_{ILC}), the pneumatic gain of the system and the wafer, which is a mass system. This is shown in Equation 5, where C_{OLC} is the outer loop controller.

$$PC = \frac{T_{ILC} C_{OLC}}{m_{wafer} s^2} \tag{5}$$

For the controller, it is decided to use a PD controller with a low pass filter. The low pass filter must be placed before 300 Hz to cancel out the coupling in the inner loop. Because of the high gain of the mass-line, it was chosen to leave out the integrator.

$$K_p = \frac{m_{wafer} \omega_{bw}^2}{k_{pn} * 4}; \tag{6}$$

The gain of the system was calculated using Equation 6. To start, the pneumatic gain k_{pn} values calculated by Krijnen were used. This gives an initial place to start after which the controller has been tuned iteratively. After the initial measurement, the new controller gain could be calculated to compensate for the lower pneumatic gain. Figure 25, shows the closed-loop response of the system. The measurements for the cross-coupling between the x and y-axis are insignificant and thus not presented in the frequency domain. The error of the x and y-axis during tracking is presented, in Figure 27.

TABLE IV
OUTER LOOP CONTROLLER PROPERTIES.

Parameter	Translation	Rotation
K_p	0.207	2.842
f_d	2.5	2.5
f_t	40	40
f_f	150	200

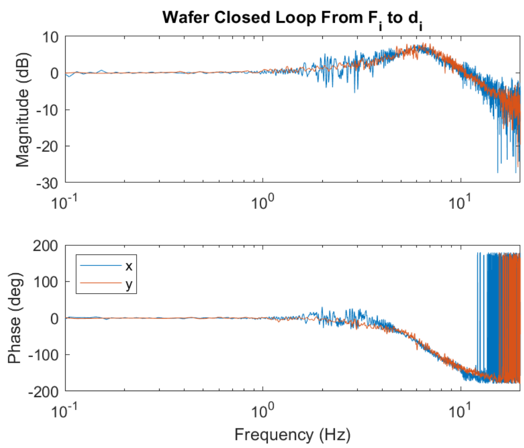

Fig. 25. The closed loop response of from the position set point to the measured position for the translations.

D. Performance

After tuning the controller for the inner loop, outer loop and pressure the performance of the positioning of the wafer has been measured. The error at steady state is shown in Figure 26. The periodic movement is caused by the correlation between the rotation and translational degrees of freedom. This is expected as the dummy wafer is not perfectly round.

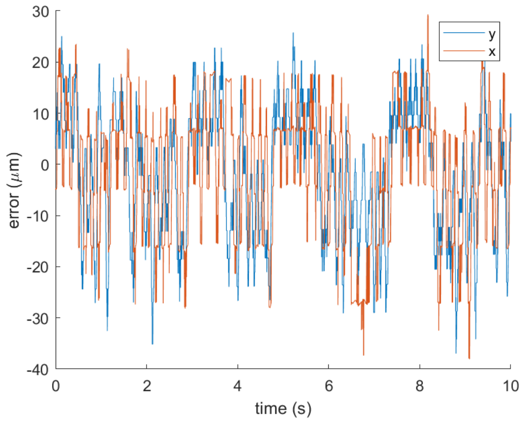

Fig. 26. The steady state error during control of the wafer in x and y

TABLE V
OUTER LOOP CONTROLLER PROPERTIES.

DOF	RMS error
x	12.4 μm
y	12.9 μm
Rz	3.1 mrad

Furthermore, when tracking a sinewave with an amplitude of 0.33 millimeters at 0.5 Hz, the RMS error of x and y remained under 9 μm. During the tracking, less rotation was observed.

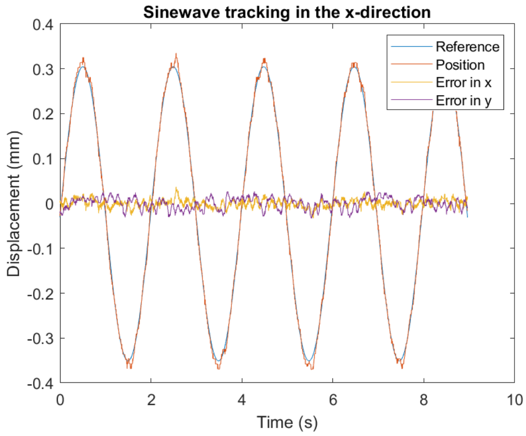

Fig. 27. The control strategy for the flowerbed. [6]

VII. CONCLUSION

The push for thinner and wider wafers has also resulted in the need for contactless handling of the substrates. The flowerbed and other concepts were developed for this purpose using the air-bearing concept. This paper has presented the air-bearing contactless wafer handling system where the wafer's position is sensed without any alterations to the wafer.

The performance of the inner loop has been improved from 233 Hz to 300 Hz by improving the controller. This is an improvement of almost 30 percent. The inner loop creates a stable platform for the outer loop controller which controls the position of the wafer. External disturbances are handled in the inner loop, as the air does not transmit the vibrations from the floor.

With the use of three Charge-Coupled Devices (CCD) the position of the wafer could be measured by detecting the edge of the wafer. This is done without any alteration of the wafer. The CCD sensors have a resolution of 5.5 um.

Due to the unforeseen lowering of the pneumatic gain, the bandwidth for control has not been improved. However, the wafer has been controlled using the new sensors design, resulting in a bandwidth of 10 Hz. The wafer can be positioned with a high accuracy of 13 μm RMS, which is under 3 resolution counts of the sensor. This showcases the high precision positioning capability of the flowerbed.

Further improvement of the inner loop could be achieved without the redesign of the actuator. This improvement can be made by laminating the mover such that the effect from the eddy current is removed. If lamination is not an option switching to flux feedback could remove the effect from the eddy currents, which are lowering the phase and thus the bandwidth. Also decoupling filters could be used to improve the closed loop sensitivity function of the innter loop. But, even in the current state the Inner Loop is no longer limiting the performance of the Outer Loop.

The resolution of the CCD could be improved to sub-micrometer resolution using sub-pixel interpolation techniques. Also using improved hardware is possible to increase the sampling frequency of the current CCD from 320 Hz to 1.2 kHz.

REFERENCES

[1] Fraunhofer, ISE: Photovoltaics report, February 2018.
[2] S. Carey, et al. Yield Impact of Backside Metal-Ion Contamination. Solid State Phenomena, vol. 187, Trans Tech Publications, 2012.
[3] R. Jansen, Actuation System for the FLowerbed, Master's thesis, Delft University of Technology, 2018.
[4] J. Wesselingh, Contactless Positioning using an Active Air Film. PhD thesis, Delft University of Technology, 2011
[5] P. H. Vuong, Air-Based Contactless Actuation System for Thin Substrates. PhD thesis, Delft University of Technology, 2016.
[6] M. Krijnen, Control system design for a contactless actuation system. Master's thesis, Delft University of Technology, 2016.
[7] E.P. Vagher, Contactless Passive Transport of Thin Solar Cells . Master's thesis, Delft University of Technology, 2016.
[8] J. Snieder, Development of an Air-Based Contactless Transport Demonstrator. Masters thesis, Delft University of Technology, 2017.
[9] Y. Voorrips, The design of a distributed sensing system for contactless substrate transport. Masters thesis, Delft University of Technology, 2017.
[10] N. Verbruggen, Air-Based Contactless Positioning of Thing Substrates, Master's thesis, Delft University of Technology, 2018.
[11] A. Katalenic, Control of reluctance actuators for high-precision positioning. Eindhoven: Technische Universiteit Eindhoven, 2013.
[12] E.P. Vagher, Contactless Passive Transport of Thin Solar Cells, Master's thesis, Delft University of Technology, 2016.

[13] J. Fischer et al, Simple Methods of Edge Position Measurement Using Shadow Projected on CCD Sensor, Czech Technical University, 2003.
[14] 12-2019, http://www.silicon-wafer.co.jp/semispec.htm
[15] L. Chang-Ming et al, Sub-pixel Edge Detection Based on Polynomial Fitting for Line-matrix CCD Image, Weifang University, 2009.
[16] X. Guo-Sheng, Linear Array CCD Image Sub-pixel Edge Detection Based on Wavelet Transform, Weigang University, 2009.
[17] J. FISCHER et al, Precise subpixel position measurement with linear interpolation of CMOS sensor image data, Czech Technical University, 2005
[18] M. Hagara, O. Kulla, Edge detection with sub-pixel accuracy based on approximation of edge with Erf function, Radioengineering, 2011.

6
Conclusions and Recommendations

6.1. Conclusions

The push for thinner and wider wafers has also resulted in the need for contactless handling of the substrates. The flowerbed and other concepts were developed for this purpose using the air-bearing concept. This paper has presented the air-bearing contactless wafer handling system where the wafer's position is sensed without any alterations to the wafer. In this chapter, the conclusions are given on the actuator and sensing system.

6.1.1. Conclusions on the flowerbed actuator

The performance of the inner loop has been improved from 233 Hz to 300 Hz by improving the controller. This is an improvement of almost 30 percent. The inner loop creates a stable platform for the outer loop controller which controls the position of the wafer. The floor vibrations are handled in the inner loop.

The delay sources in the system have been investigated. The delay of the eddy current sensors, ADC, amplifier, and the actuator has been identified. The main contributions for the delay are the eddy currents and the sampling time delay.

The pneumatic gain which was validated by Krijnen en Vuong, could not be reached without contact. Multiple factors play a role here, the flowerbed has been taken apart and reassembled by Jansen to replace the actuators. Upon close inspection, it appears that multiple flowers are out of alignment. Furthermore, the supply pressure is leaking between flowers and the pressure chamber.

6.1.2. Conclusions on the sensing system

The edge of the wafer could be measured using a Charge-Coupled Device (CCD) without any alterations to the wafer.

The performance of the Charge-Coupled Device (CCD) was tested for linearity and drift. In steady-state this resulted in an error of 3.0 $/mu$ RMS.

The CCD sensors have been implemented in the contactless actuation stage making it possible to close the loop. The wafer has been controlled using the new sensors design, resulting in a bandwidth of 10 Hz. The wafer can be positioned with a high accuracy of 13 μm RMS, which is under 3 resolution counts of the sensor.

6.2. Recommendations

For further work the following recommendations are made:

- Further improvement of the inner loop could be achieved without the redesign of the actuator. This improvement can be made by laminating the mover such that the effect from the eddy current is removed. If lamination is not an option switching to flux feedback could remove the effect from the eddy currents, which are lowering the phase and thus the bandwidth. Without the effects of the eddy current, the differentiating action could be reduced and hence the noise attenuation and reference tracking will improve.

- The performance of the current CCD sensors could be improved by using sub-pixel interpolation This would lower the resolution of 5.5 um, to sub-micrometer. Also using a faster ADC the sampling frequency of the current CCD could be improved from 320 Hz to 1.2 kHz.
- The performance of the outer loop is limited by the offset of the flowers during steady-state control. This limits the range of the movable plate without contact. During the experiments, the offset limited the range of the movable plate by 30 percent. It was observed that the offset changes with the pressure.
- The performance of the flowerbed could be increased by using the high stiffness of piezo actuators. If the suspension mode could be placed at high frequencies a cascaded control structure may not be necessary.

A
Matlab code

In this chapter the matlab code is presented to calculate the numerator and denominator values used in LabVIEW.

```
%% Rico Hooijschuur
% Calculations for the flowerbed controllers
% Nov - 2019

%% ILC ~ 300 Hz
s = tf('s');
Ts = 50e-6;            % Sampling Time
Kp = 15.2;             % Gain
wi = 10*2*pi;          % Integrator
wd = 50*2*pi;          % Differentiator
wt = 2000*2*pi;        % Taming action
wf = 2500*2*pi;        % Low Pass filter


C = Kp * (1 + wi/s)*(s/wd + 1)/(s/wt + 1) / (s/wf + 1);

Cd = c2d(C,Ts,'tustin');
[num,den] = tfdata(Cd); num = num{1}; den = den{1};

%% ILC FF Design 300 Hz and split up TF to fix LabVIEW

s = tf('s');
K = 0.367663062167172;
w1 = 2*pi*48.6;
w2 = 2*pi*59.89;
w3 = 2*pi*75.44;
d1 = 0.052;
d2 = 0.065;
d3 = 0.085;
wfp = 2*pi*300;

% Estimation of the Plant with damped zero
d2 = 1.0;
G = -K*((s/w2)^2 + 2*s*d2/w2 + 1)/((s/w1)^2 + 2*s*d1/w1 + 1)/((s/w3)^2 + 2*s*d3/w3 +
    1)/(s/wfp + 1);

% FeedForward controller
```

```
wf = 2*pi*300;
FF = 1/G/((s/wf)^2 + 2*s/wf + 1)/((s/wf)^2 + 2*s/wf + 1);

[num,den] = tfdata(c2d(FF,0.5e-4,'tustin'));
num = num{1};den = den{1};

% Split up feedforward controller to fix internal state corruption in
% labview
FF1 = -K*((s/w2)^2 + 2*s*d2/w2 + 1)/((s/w1)^2 + 2*s*d1/w1 + 1);
FF1 = 1/FF1;
[num1,den1] = tfdata(c2d(FF1,0.5e-4,'tustin'));

num1 = num1{1};den1 = den1{1};
FF2 = 1/((s/w3)^2 + 2*s*d3/w3 + 1)/(s/wfp + 1);
FF2 = 1/FF2/((s/wf)^2 + 2*s/wf + 1)/((s/wf)^2 + 2*s/wf + 1);
[num2,den2] = tfdata(c2d(FF2,0.5e-4,'tustin'));

num2 = num2{1};den2 = den2{1};
%% CCD Kinematics

% Converting to mm
p1 = d1 * 0.0055;
p2 = d2* 0.0055;
p3 = d3* 0.0055;

% Kinematics
Y = (p2+p3)/2;
X = p1 + 100 - sqrt (10000 - Y^2);
Rz = (p2-p3)/41.5;
%% OLC Translation 10 Hz
s = tf('s');
kpx = 0.063*(2*pi*10)^2/(300 * 4); % m * s^2 / (kpn * 4), Kpn = 1.4 mN/um = 1400 mN
    /mm

% PD COntroller + LPF 150 Hz
Col = kpx * (s/2/pi/2.5 + 1)/(s/2/pi/40 + 1) / (s/2/pi/150 + 1);
Cold = c2d(Col,1/300,'tustin');

[num,den] = tfdata(Cold);
num = num{1};den = den{1};
%% OLC Rotation 0.5 Hz
s = tf('s');
kpz = 0.063*(2*pi*10)^2/(1400 * 4) * 2^6; % m * s^2 / (kpn * 4), Kpn = 1.4 mN/um =
    1400 mN/mm

% PD COntroller + LPF 150 Hz
Col = kpz * (s/2/pi/2.5 + 1)/(s/2/pi/40 + 1) / (s/2/pi/150 + 1);
Cold = c2d(Col,1/300,'tustin');

[num,den] = tfdata(Cold);
num = num{1};den = den{1};
%% Pressure Control
scale = 1;
Tp = 100e-6;

% Vacuum
```

```
Kv = -1000;
wv = 2*pi*150;
LPv = tf(1,[1/wv 1]);
LPv_c = Kv/scale*LPv*LPv;
LPv_d = c2d(LPv_c,Tp,'tustin');
[numv,denv] = tfdata(LPv_d); numv = numv{1}; denv = denv{1};

% Pressure
KP = 5000;
wP = 2*pi*90;
LPP = tf(1,[1/wP 1]);
LPP_c = KP/scale*LPP*LPP;
LPP_d = c2d(LPP_c,Tp,'tustin');
[numP,denP] = tfdata(LPP_d); numP = numP{1}; denP = denP{1};
```

B

CCD performance analysis setup

The stage used for the performance analysis of the stage is shown in Figure B.1. The stage is a Thorlabs DDSM100, it uses a optical encoder to measure its with a resolution of 0.1 um. This is used to validate the position of the senor, as shown in Chapter 5.

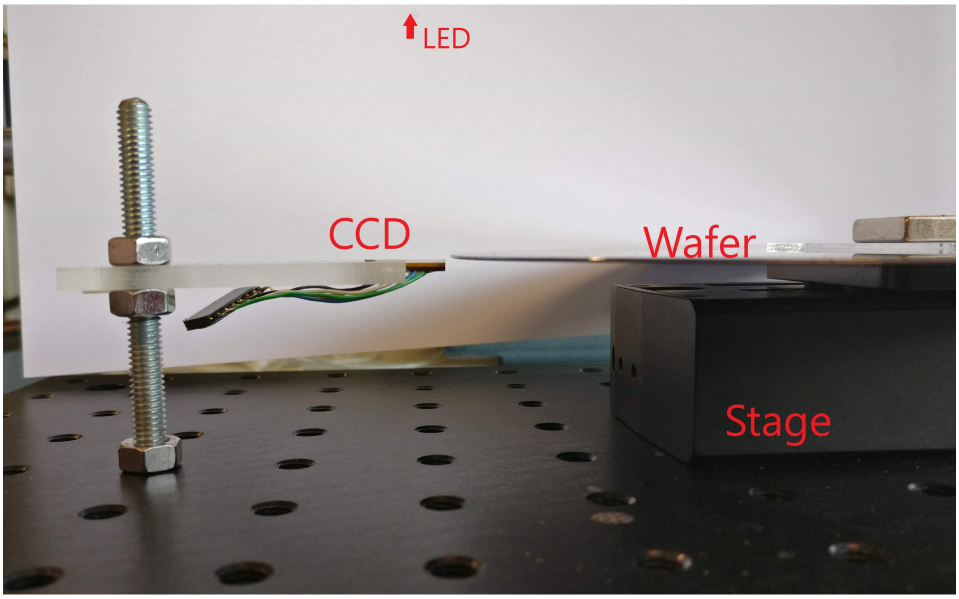

Figure B.1: The overview of the validation stage

C

The Setup

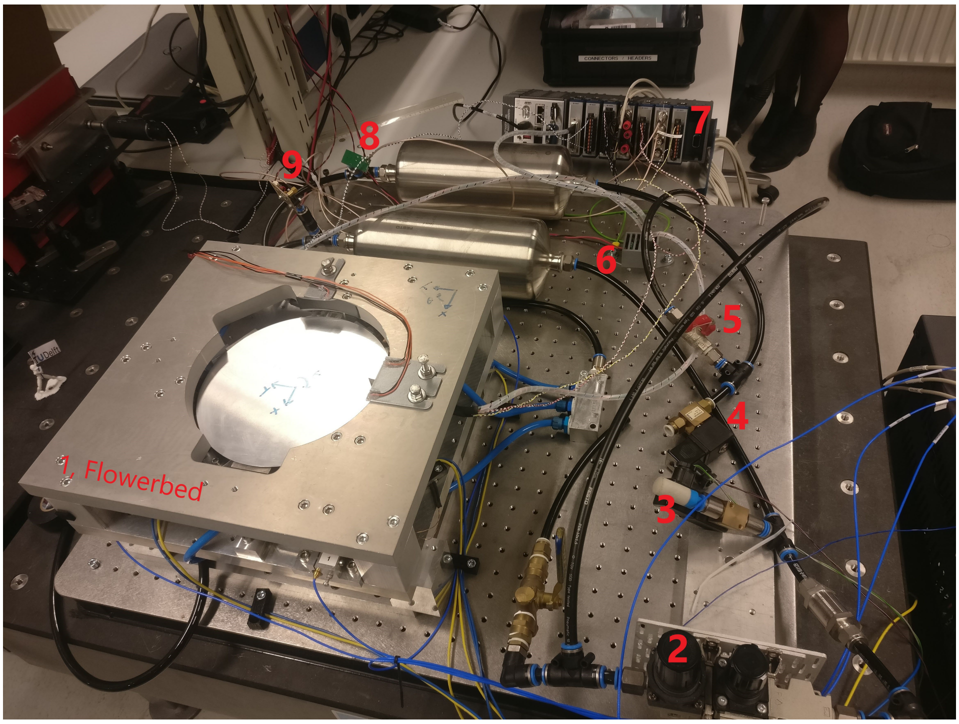

Figure C.1: The overview of the setup with all its components

1. The flowerbed, Contactless actuation system
2. Supply pressure
3. Supply pressure valve
4. Vacuum supply valve
5. Vacuum supply
6. 5v to 3.3v converter
7. The CompactRio FPGA
8. The vacuum sensor
9. The pressure sensor

Bibliography

[1] Fraunhofer, ISE: Photovoltaics report, February 2018.

[2] S. Carey, et al. "Yield Impact of Backside Metal-Ion Contamination." Solid State Phenomena, vol. 187, Trans Tech Publications, 2012.

[3] Roy Jansen, Actuation System for the FLowerbed, Master's thesis, Delft University of Technology, 2018.

[4] J. Wesselingh, Contactless Positioning using an Active Air Film. PhD thesis, Delft University of Technology, 2011

[5] P. H. Vuong, Air-Based Contactless Actuation System for Thin Substrates. PhD thesis, Delft University of Technology, 2016.

[6] M. Krijnen, Control system design for a contactless actuation system. Master's thesis, Delft University of Technology, 2016.

[7] E.P. Vagher, Contactless Passive Transport of Thin Solar Cells . Master's thesis, Delft University of Technology, 2016.

[8] J. Snieder, Development of an Air-Based Contactless Transport Demonstrator. Master's thesis, Delft University of Technology, 2017.

[9] Y. Voorrips, The design of a distributed sensing system for contactless substrate transport. Master's thesis, Delft University of Technology, 2017.

[10] N. Verbruggen, Air-Based Contactless Positioning of Thing Substrates, Master's thesis, Delft University of Technology, 2018.

[11] A. Katalenic, Control of reluctance actuators for high-precision positioning. Eindhoven: Technische Universiteit Eindhoven, 2013.

[12] E.P. Vagher, Contactless Passive Transport of Thin Solar Cells, Master's thesis, Delft University of Technology, 2016.

[13] G. Mok, The design of a planar precision stage using cost effective optical mouse sensors, Master's thesis, Delft University of Technology, 2015.

[14] 12-2019, http://www.silicon-wafer.co.jp/semispec.htm

[15] L. Chang-Ming et al, Sub-pixel Edge Detection Based on Polynomial Fitting for Line-matrix CCD Image, Weifang University, 2009.

[16] X. Guo-Sheng, Linear Array CCD Image Sub-pixel Edge Detection Based on Wavelet Transform, Weigang University, 2009.

[17] J. FISCHER et al, Precise subpixel position measurement with linear interpolation of CMOS sensor image data, Czech Technical University, 2005

[18] M. Hagara, O. Kulla, Edge detection with sub-pixel accuracy based on approximation of edge with Erf function, Radioengineering, 2011.